

# 1 Real-Time Estimation of Airflow Vector based on Lidar 2 Observations for Preview Control

3 Ryota Kikuchi<sup>1,2</sup>, Takashi Misaka<sup>3</sup>, Shigeru Obayashi<sup>4</sup>, Hamaki Inokuchi<sup>2</sup>  
4

5 <sup>1</sup>DoerResearch Inc., Chiba 260-0013, Japan

6 <sup>2</sup>Japan Aerospace Exploration Agency, Tokyo 181-0015, Japan

7 <sup>3</sup>National Institute of Advanced Industrial Science and Technology, Ibaraki 305-8564, Japan

8 <sup>4</sup>Tohoku University, Miyagi 980-8577, Japan  
9

10 *Correspondence to:* Ryota Kikuchi (Email: kikuchi-ryota@doerresearch.com)

11 **Abstract.** As part of control techniques, gust-alleviation systems using airborne Doppler Lidar technology are  
12 expected to enhance aviation safety by significantly reducing the risk of turbulence-related accidents. Accurate  
13 measurement and estimation of the vertical wind velocity are very important in the successful implementation of such  
14 systems. An estimation algorithm for the airflow vector based on data from airborne Lidars is proposed and  
15 investigated for preview control to prevent turbulence-induced aircraft accidents in flight. An existing technique —  
16 simple vector conversion— assumes that the wind field between the Lidars is homogeneous, but this assumption fails  
17 when turbulence occurs due to a large wind-velocity fluctuation. The proposed algorithm stores the line-of-sight (LOS)  
18 wind data at every moment and uses recent and past LOS wind data to estimate the airflow vector and to extrapolate  
19 the wind field between the airborne twin Lidars without the assumption of homogeneity. Two numerical  
20 experiments—using the ideal vortex model and numerical weather prediction, respectively—were conducted to  
21 evaluate the estimation performance of the proposed method. The proposed method has much better performance than  
22 simple vector conversion in both experiments, and it can estimate accurate two-dimensional wind-field distributions,  
23 unlike simple vector conversion. The estimation performance and the computational cost of the proposed method can  
24 satisfy the performance demand for preview control.

## 25 1 Introduction

26 Atmospheric turbulence poses a potential risk to aircraft operation. Statistics reported by Boeing (2018) show  
27 that 322 non-fatal and 51 fatal accidents occurred worldwide in commercial jet flights from 2009 through 2018. Of  
28 the fatal accidents, the largest proportion (25.5%) were due to Loss of Control-In Flight (LOC-I). The International  
29 Air Transportation Association (2016) shows that LOC-I frequently occurs when the aircraft speed is well below the  
30 stall speed; in conjunction with weather conditions, low speed is the most common factor in LOC-I accidents. Forty-  
31 two percent of LOC-I accidents occurred under degraded meteorological conditions affecting aircraft speed, in  
32 particular strong wind shear and atmospheric turbulence.

33 For both fatal and non-fatal aircraft accidents, the impact of atmospheric turbulence can be significant. The  
34 Japan Transport Safety Board has stated that accidents caused by turbulence accounted for 48% of non-fatal aircraft  
35 accidents in Japan involving commercial airplanes from 2003-2012. An increase in the rate of accidents related to  
36 turbulence was reported by the Federal Aviation Administration in 2006, Kim and Chun in 2011, and Williams in  
37 2017. Accidents caused by convective systems such as cumulonimbus clouds have decreased owing to advances in  
38 airborne Radar (Airbus, 2020; Sermi et al. 2015). However, non-cloud atmospheric turbulence, called clear-air  
39 turbulence (CAT), cannot be detected by Radar, as reported by Soreide et al., 2000; Barny, 2012; and Inokuchi et al.,  
40 2009. Airborne CAT-observation systems to minimize risks of turbulence-related accidents are essential for aviation  
41 safety.

42 Numerical weather prediction (NWP), which is an essential tool for aircraft operation, can forecast weather  
43 conditions for days and even weeks in advance and output broader-area weather information than can Radar or Lidar.  
44 However, NWP cannot explicitly resolve disturbances as small as most turbulence, leading to a very large predictive  
45 uncertainty (Sharman et al. 2006, Kim et al. 2011). Therefore, some researchers have developed an alternative  
46 approach that predicts turbulence potential by calculating turbulence indicators from NWP results; for example,  
47 Sharman et al. (2006) have developed an approach called graphical turbulence guidance (GTG) that combines such  
48 indicators. The turbulence potential can also be used to determine operational flight routes (Kim et al. 2015), but it  
49 has a large spatio-temporal gap on the scale of aircraft motion because it is based on NWP results such as the meso-  
50 scale model. It thus provides insufficient information to implement turbulence avoidance on aircraft in flight.

51 Recently, airborne Doppler Lidar has been developed by Soreide et al., 2000; Barny, 2012; Inokuchi et al.,  
52 2009; Machida, 2017; and Inokuchi and Akiyama, 2019. Emitted laser light is scattered by fine aerosol particles in  
53 the atmosphere; the back-scattered light is condensed by telescopes and received by an optical transceiver. Since the  
54 wavelength of the received light varies according to the velocity of the aerosol particles due to the Doppler effect,  
55 wind speed can be calculated by comparing this wavelength with that of the received light (Inokuchi and Akiyama,  
56 2019). However, when rain is too heavy, the backscattering signal is weakened due to strong attenuation by raindrops  
57 and a decrease in aerosols (Wei et. al 2019), making it difficult to measure the wind velocity at a distance. Japan  
58 Aerospace Exploration Agency (JAXA) is researching and developing a coherent Doppler Lidar capable of remotely  
59 detecting air turbulence in clear-air conditions, and has conducted a flight demonstration of a Lidar system that can  
60 provide turbulence information to pilots (Inokuchi et al., 2009; Machida, 2017; Inokuchi and Akiyama, 2019).  
61 Inokuchi et al. (2012) have shown observationally that airborne Doppler Lidar can detect CAT in front of an aircraft  
62 in flight at altitudes of 3,200 m; the Lidar information can be detected 30 seconds before the turbulence affects the  
63 aircraft. The aircraft's flight speed in the test was 320 kt (160 m/s), so it detected CAT from a distance of about 4.8  
64 km.

65  
66  
67 Based on advance airflow information, flight demonstrations have been carried out with the aim of providing pilots  
68 with the information they need to make decisions: whether to change course to avoid wind shear, and whether to turn  
69 on seatbelt-sign lighting during cruise and altitude changes (Inokuchi and Akiyama, 2019). Although Lidar systems

70 are useful for providing onboard wind information to pilots, avoiding turbulence at high altitudes is difficult as the  
71 range of detection that facilitates pilots to be warned is short (Hamada, 2019). Gathering such information involves  
72 emitting a laser beam and receiving the scattered light from aerosol particles that are much smaller than precipitation  
73 droplets in the air. Therefore, when the number of aerosol particles that emit scattered light is small, it is difficult to  
74 measure wind information at a distance. Furthermore, as altitude increases, the aerosol density decreases, and the  
75 observation range tends to decrease accordingly. The maximum observation range and aerosol density measured at  
76 each altitude are shown in Inokuchi and Akiyama, 2019.

77 Advance knowledge of turbulent atmospheric conditions would improve the performance of automatic  
78 aircraft-vibration reduction systems. Automatic control to alleviate aircraft vibration is called gust-alleviation and has  
79 been studied since the 1970s, mostly with only the help of feedback sensors such as inertial measurement units (Regan  
80 and Jutte, 2012). Recently, methods of reducing the vibrations due to turbulence with the help of preview controlling  
81 based on airborne Lidar observation have been reported by Schmitt et al., 2007; Fezans et al., 2019; and Hamada,  
82 2019. The aim of the Aircraft Wing with Advanced Technology Operation (AWIATOR) project is the development  
83 of new direct-lift control devices and a Lidar system for turbulence measurement (Schmitt et al., 2007). Another  
84 project—“Demonstration of Lidar-based CAT detection” (DELICAT) (Barny, 2012)—developed airborne ultraviolet  
85 Lidar for gust and turbulence measurements. The test flights were carried out using an Airbus 340 aircraft equipped  
86 with ultraviolet Lidar. In both the AWIATOR and the DELICAT experiments, the measurement range was short,  
87 because the Lidar was developed for controlling the aircraft automatically.

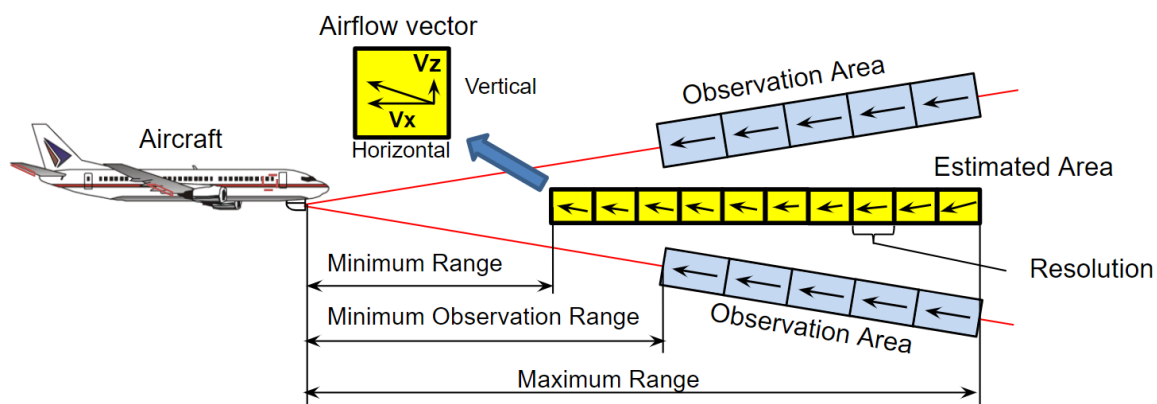
88 In order to implement an airborne Doppler Lidar gust-alleviation system successfully, it is very important to  
89 measure the vertical wind velocity accurately. Both horizontal and vertical winds affect aircraft motion, but the effect  
90 of changing the vertical wind velocity is greater. This is because the effect of modifying the angle of attack is relatively  
91 larger than the effect of changing the horizontal wind velocity, which affects only the airspeed (Fezans et al., 2019).  
92 However, a fixed single Doppler Lidar system can only detect the line-of-sight (LOS) wind, providing a one-  
93 dimensional piece of information; the vertical wind velocity in front of the aircraft cannot be measured by such a  
94 system (Hamada, 2019). It is necessary to perform the Lidar measurements in two directions, upward and downward,  
95 to obtain the vertical wind velocity (Neininger, 2017). Figure 1 shows a representation of this concept. The vertical  
96 wind-velocity vector is generated from the differences between the upward and downward LOS winds by using simple  
97 vector conversion. Unfortunately, this method is incapable of estimating the vertical wind velocity with high accuracy  
98 to control the aircraft automatically because the technique assumes homogeneity between the upward and downward  
99 Lidars (Fezans et al., 2019). In this study, a fully turbulent field with atmospheric turbulence and gusts is considered;  
100 under these conditions, it is difficult to estimate the vertical wind velocity with high accuracy using simple vector  
101 conversion. In particular, the estimation accuracy of the vertical wind velocity rapidly worsens when the estimation  
102 position is located farther ahead from the aircraft.

103 In addition, actual Lidar observations involve errors, noise, and loss of data, with negative effects on aircraft  
104 control, as reported by Misaka et al. (2015); these problems are worse at higher altitudes, where the aerosol density is  
105 smaller than it is at lower ones. Misaka et al. (2015) proposed a filtering algorithm based on a simple Kalman filter to  
106 remove wind-velocity errors from Lidar measurements. For preview control, it is essential to deal with the Lidar errors,

107 noise and loss of data more carefully. An accurate airflow vector estimation method and an efficient real-time filtering  
108 algorithm are required.

109 In this study, an estimation method and an airflow-vector filtering algorithm are proposed for preview control  
110 to prevent turbulence-induced aircraft accidents. The method works for both horizontally and vertically directed winds,  
111 and uses both upward and downward Lidars. (In this study, “horizontal wind” means any headwind/tailwind  
112 component that does not include the crosswind component.) The Lidar system in this paper is that also used by JAXA  
113 in its ongoing “Lidar-based gust alleviation control” research project. The Lidars are assumed to be compliant with  
114 the specifications for preview control currently under development by the JAXA. The proposed algorithm stores the  
115 LOS wind data continually and uses recent and past LOS wind data to estimate the airflow vector and the wind field  
116 between Lidars, whereas simple vector conversion utilizes only recent LOS wind data. The airflow vector is calculated  
117 by using wind data extrapolated from the horizontal and vertical wind components; the estimation accuracy of the  
118 airflow vector in front of the aircraft is improved by using such extrapolated wind data because the region between  
119 the Lidars represents a non-homogeneous one. A polynomial expression is used to extrapolate the wind field. In  
120 addition, the proposed method can estimate the two-dimensional distribution of the wind field between the Lidars,  
121 which simple vector conversion cannot.

122 Two test configurations—an ideal vortex flow field and a weather field—are calculated by an NWP system  
123 and utilized to evaluate the performance of the airflow vector. These experiments generate a large number of pseudo-  
124 Lidar measurements along flight routes from the reference wind field for evaluation of the estimated performance.  
125 Comparing the prediction results with the reference wind field can confirm all the wind-field values.



126

127

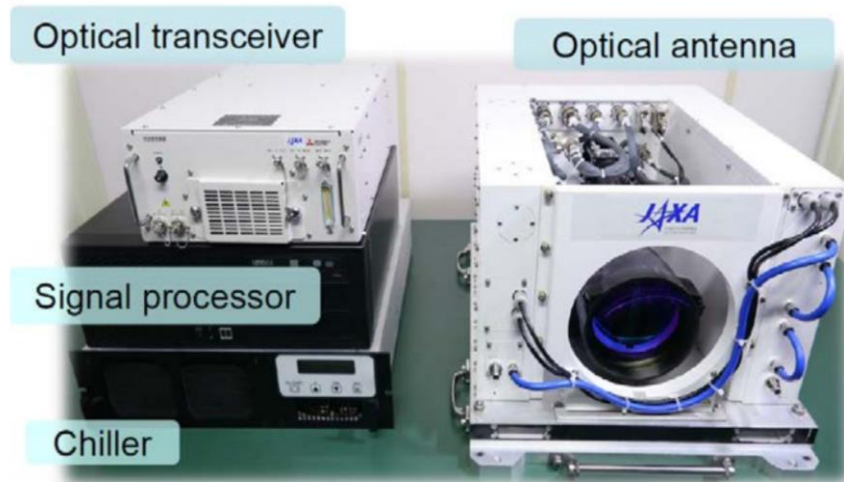
Fig. 1 Concept of the airborne Lidars observation system

## 128 2 Methods

### 129 2.1 Airborne Lidar Specifications

130 The airborne Lidar observation system currently under development by JAXA for preview control to prevent  
131 turbulence-induced aircraft accidents is shown in this section. This system has airborne Lidars that are aiming upwards  
132 and downwards; the angle between them is 20 degrees, that is, 10 degrees between the horizontal line and each Lidar.

133 The Lidar sensor is shown in Fig. 2; its specifications are given in Table 1 (Inokuchi and Akiyama 2019). Laser pulses  
 134 generated by an optical transceiver are amplified by optical amplifiers (Sakimura et. al. 2013) incorporated into an  
 135 optical antenna and radiated into the atmosphere from optical telescopes. The heat generated by the optical amplifiers  
 136 is dissipated by a water-cooled chiller unit. The optical antenna is equipped with a 150 mm large-aperture telescope  
 137 for long range observations and a 50 mm small-aperture telescope for vector conversion of short-range observations.  
 138 Each Lidar measures the LOS wind velocity with an observational accuracy of  $\pm .09 \text{ m s}^{-1}$ ; the paired values are used  
 139 to estimate the airflow vector in the region between the Lidars. The observational resolution of each Lidar is  
 140 approximately 25 m. There are additional performance requirements for preview control: the estimation frequency  
 141 and estimation accuracy of vertical wind velocity. The frequency of estimation must be more than 5 Hz, and the  
 142 estimation accuracy of the vertical wind velocity must be better than  $2.6 \text{ m s}^{-1}$  in the LOS distance of 500 m. The  
 143 control requirements are the conditions that are necessary for halving the peak variation in acceleration by control.  
 144 This value has been specified using control simulations (Hamada, 2019), and Monte Carlo simulations have also been  
 145 performed.



146  
 147 **Fig. 2 Coherent Doppler Lidar used in this work**

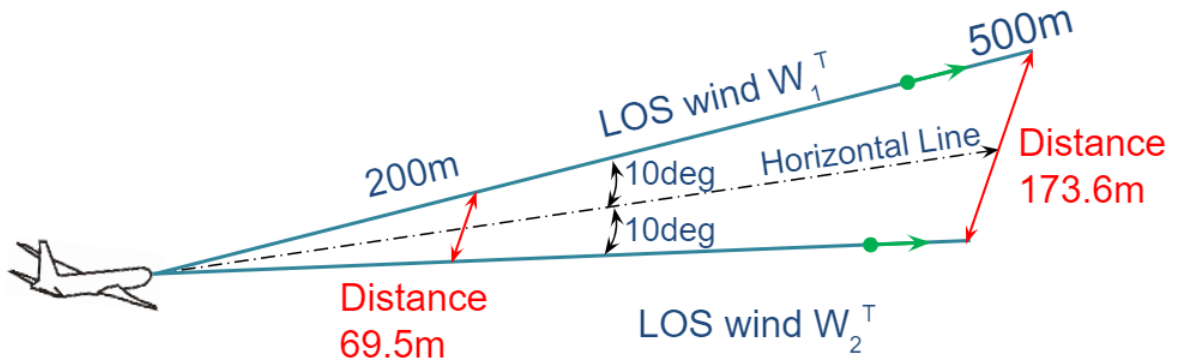
148  
 149 **Table 1. Coherent Doppler Lidar Specifications**

Laser Wavelength	1.55 $\mu\text{m}$
Laser Output	3.3 W
Pulse Repetition Frequency	1,000 Hz
Laser Beam Diameter	150, 50 mm
System Weight	83.7 kg
Power Consumption	936 W
Data Rate	5 Hz

150 Next, an existing technique for estimating the airflow vector from a pair of LOS wind values is reviewed.  
 151 The airflow vector in the region between the upward and downward Lidars is conventionally estimated via simple  
 152 vector conversion. This procedure is similar in concept to the vertical azimuth display approach used in general ground  
 153 Lidar systems (Newsom et al., 2017). The simple vector conversion is given by

$$\begin{aligned} u_x^T &= \frac{(W_1^T + W_2^T)}{2\cos\theta}, \\ u_z^T &= \frac{(W_1^T - W_2^T)}{2\sin\theta}, \end{aligned} \quad (1)$$

154 where  $u_x^T$  and  $u_z^T$  are the horizontal and vertical wind velocity measurements at the observation time  $T$ ;  $W_1^T$  and  
 155  $W_2^T$  are the LOS wind velocities of the upward and downward directed Lidars at the observation time  $T$ ; and  $\theta$  is the  
 156 angle between the horizontal line and each Lidar, which is 10 degrees in this study. The simple vector conversion  
 157 assumes that the wind-field region between the Lidars is homogeneous (Newsom et al., 2017). The assumption of  
 158 homogeneity seems natural: the regions between the Lidars are 69.5 m and 173.6 m at the LOS distances of 200 m  
 159 and 500 m ahead of the aircraft (Fig. 3). Nevertheless, the assumption would be wrong if a large fluctuation in wind  
 160 velocity occurs, creating turbulence. In homogenous conditions, a simple vector conversion can estimate the airflow  
 161 vector accurately; however, in non-homogenous conditions, the estimation is expected to have poor accuracy.



162  
 163 **Fig. 3 Distance to wind-field region between the Lidars for two line-of-sight (LOS) distances**

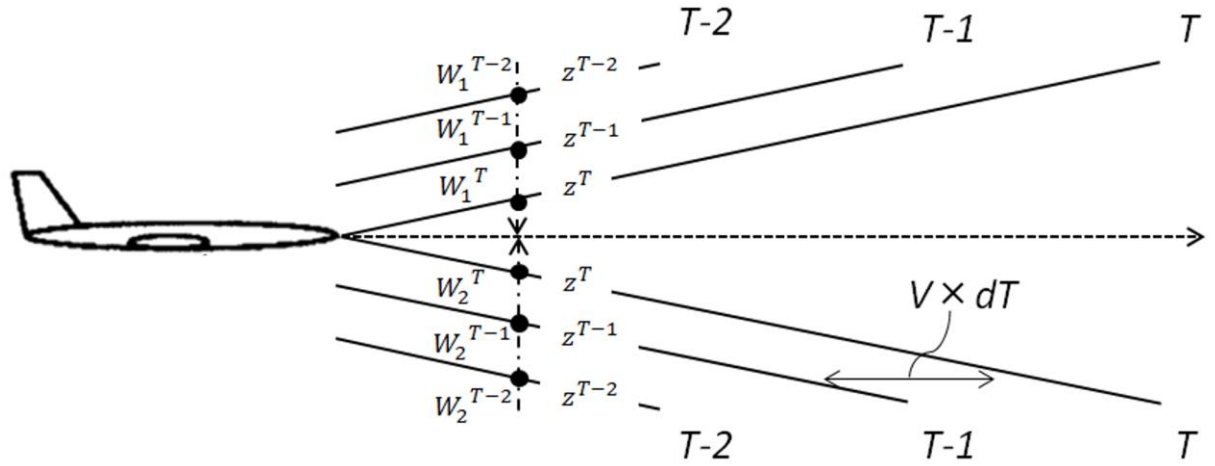
## 164 2.2 Estimation Algorithm Based on Extrapolation

165 Whereas simple vector conversion utilizes recent LOS wind data to estimate the airflow vector, our proposed  
 166 method stores the LOS wind data continuously and uses both recent and past values to extrapolate the wind field in  
 167 the region between the Lidars where it has not been directly measured. The airflow vector is then calculated from Eq.  
 168 (1) and the extrapolated horizontal and vertical components of the wind velocity. The airflow-vector estimation  
 169 accuracy far ahead of the aircraft is improved relative to simple vector conversion by using the extrapolated wind data  
 170 because the region between the upward and downward Lidars is no longer assumed to be homogeneous; our algorithm  
 171 uses a polynomial expression to extrapolate data points from both recent and past measurements, allowing it to be

172 used in non-homogenous wind fields. In addition, the proposed method can estimate the two-dimensional distribution  
 173 of the wind field between the Lidars, again unlike simple vector conversion.

174

175 Figure 4 shows the overview of the proposed estimation method when a current data point and two past data  
 176 points are used. When the aircraft speed is  $V$  and the time span of observation is  $dt$ , the airflow moves backwards at  
 177  $V \times dt$  because the aircraft is advancing. Current observation times are denoted as  $T$  and past observation times as  $T-1$   
 178 and  $T-2$ . The proposed method uses the current LOS wind values ( $W_1^T$  and  $W_2^T$ ) and the past LOS wind values ( $W_1^{T-1}$ ,  $W_2^{T-1}$   
 179 and  $W_1^{T-2}$ ,  $W_2^{T-2}$ ). The perpendicular distances between the horizontal line and each Lidar are denoted as  $z^T$ ,  
 180  $z^{T-1}$ , and  $z^{T-2}$ , respectively. Depending on the number of past LOS wind data used, the order of the polynomial  
 181 expression used in the extrapolation varies. The aerosol concentration in the upper sky is low, suggesting that there is  
 182 considerable missing data and noise. A sufficient number of past LOS wind data may not be available to estimate a  
 183 high-order polynomial expression, and this could affect the robustness of the control. For this reason, a first-degree  
 184 polynomial expression is adopted in this study and used in the least-squares method (LSM) to extrapolate the wind-  
 185 field values according at the horizontal line. The airflow vector is calculated by Eq. (1) using the extrapolated LOS  
 186 wind. The equation used in the extrapolation method is



187

188 **Fig. 4 Overview of estimation by proposed method when line-of-sight wind data from 0, 1, and 2 past time-steps  $dT$**   
 189 **are used.  $V$  = speed of aircraft;  $W_1^T$  and  $W_2^T$  = wind speeds measured at time  $T$  by the two Lidars;  $z$  = vertical distance**  
 190 **perpendicular to velocity of aircraft**

191

$$W_j'(z) = a_j z + b_j, \quad (2)$$

where

$$a_j = \frac{N \sum_{i=T-(N-1)}^T z^i W_j^i - \sum_{i=T-(N-1)}^T z^i \sum_{i=T-(N-1)}^T W_j^i}{N \sum_{i=T-(N-1)}^T (z^i)^2 - \left( \sum_{i=T-(N-1)}^T z^i \right)^2}, \quad (3)$$

$$b_j = \frac{\sum_{i=T-(N-1)}^T z^i \sum_{i=T-(N-1)}^T W_j^i - \sum_{i=T-(N-1)}^T W_j^i \sum_{i=T-(N-1)}^T z^i}{N \sum_{i=T-(N-1)}^T (z^i)^2 - \left( \sum_{i=T-(N-1)}^T z^i \right)^2}.$$

192

193

### 2.3 Filtering Error and the Lack of Wind-Velocity Data

194

195

196

197

198

199

200

201

202

203

204

205

206

207

In this study, two filtering algorithms are used to remove the error and the loss of data in airborne Lidars. First, a filtering algorithm that is a simple representation of a Kalman filter with simplified Kalman gain is used; **this filtering algorithm is described in detail in the study of Misaka et al., 2015.** The algorithm assumes that infinite variance is used to exclude outliers and loss of data. This method uses the Lidar spectrum data at each range-bin; the algorithm defines the validity of the measurements during the Lidar data peak-detection process. To identify the correct and incorrect LOS wind-velocity values, two spectrum thresholds are defined. First, the largest and second-largest spectrum values,  $k_{1st}$  and  $k_{2nd}$ , which are the Fast Fourier Transform points for the first and second spectrum peaks, respectively, are adjacent to each other; i.e., the magnitude of the distance between the largest and second-largest spectrum values in the Fast Fourier Transform is equal to one. Second, the distance between  $k_{1st}$  and the averaged spectrum peak  $k_{ave}$  is required to be less than a certain value  $k_{dif}$ , which represents the only hyper-parameter in this algorithm as well as a parameter related to smoothness.  **$k_{ave}$  is the index that conveys the location of the spectrum peak averaged in short ranges, e.g., 2–30 range-bins from the lidar origin. Figure 5 shows a conceptual explanation of the variables of simplified Kalman gain in the cases of correct measurement and of an error peak.** In this study, the filtering algorithm is carried out first when the observation data is obtained:

$$K = \begin{cases} 1 & |k_{1st} - k_{2nd}| = 1 \text{ and } |k_{1st} - k_{ave}| < k_{dif} \\ 0 & \text{Otherwise} \end{cases} \quad (4)$$



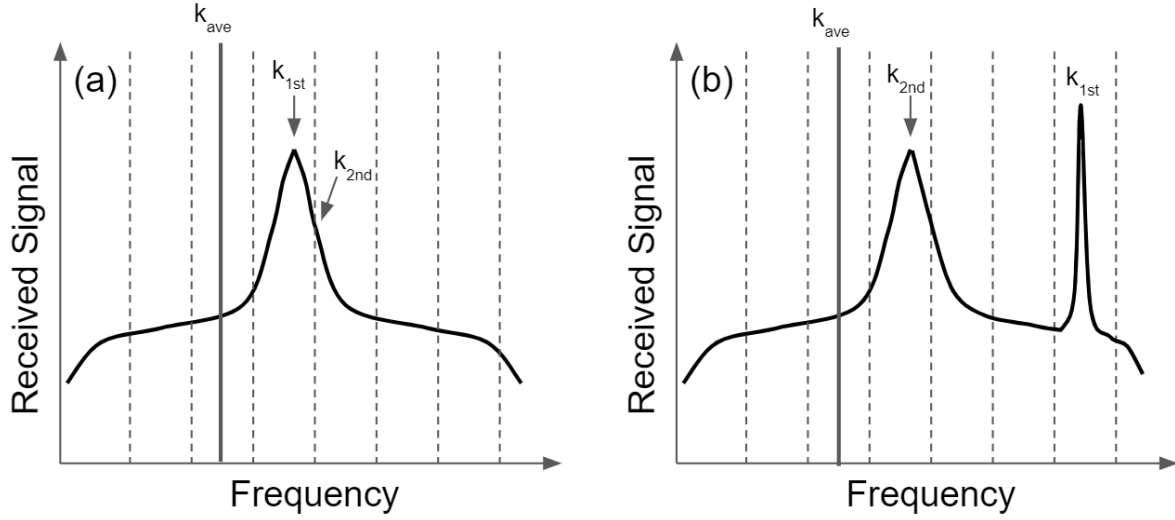


Fig. 5 Conceptual explanation of the variables of simplified Kalman gain.

(a) Correct measurement case of  $K=1$ . (b) Case with the error peak of  $K=0$

Secondly, a robust least-squares estimation, based on Tuckey's biweight methodology (Huber, 2008), is carried out to reduce the impact of the error in the LOS wind velocity. This method is based on the LOS wind data, in contrast to the spectrum data from Lidar observations in the first method. Although the filtering algorithm based on a simple Kalman filter can remove the error from the Lidar spectrum data, error filtering via this algorithm is not perfect despite being useful. As error data can be a reason for miscontrol, it is essential to deal with the error and the loss of data of the Lidars more carefully when the filtering algorithm is used for the preview control. Therefore, the robustness of the estimated airflow vector is secured by combining the simple Kalman filtering algorithm with the results of robust LSM, using Eqs. (2) and (3). In addition, the robust LSM estimation can employ the extrapolation algorithm effectively as per Eqs. (2) and (3). Therefore, a simpler and more robust algorithm is provided. Figure 6 explains the concept behind Tuckey's biweight methodology as applied to Lidar. The fundamental principle involves comparing the observed LOS wind values with the estimated ones from the polynomial expression used in the LSM. In the 1st step, the LOS wind is estimated using the general LSM (Eq. (2)). In the 2nd step, the difference  $d_j^T$  between the observed LOS wind value and that estimated from the polynomial expression is found:

$$d_j^T = W_j^T - (a_j z + b_j). \quad (5)$$

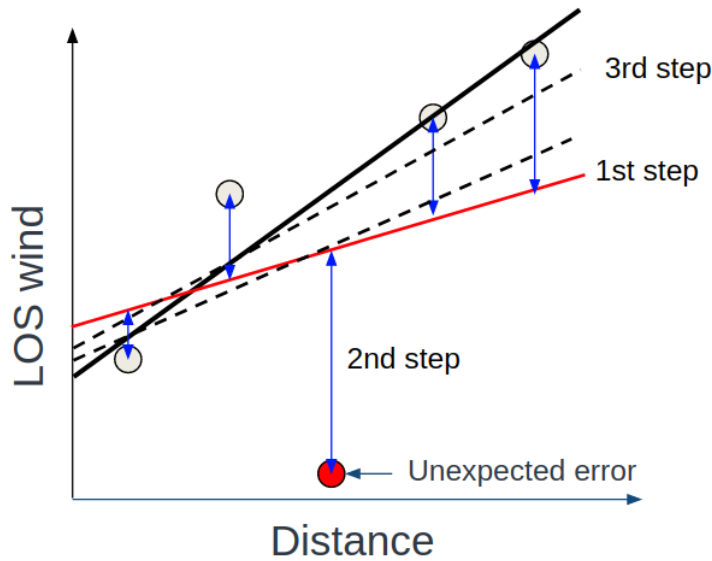
A permissible difference range  $L$  is defined and weights  $w_j^T(d_j^T)$  are calculated depending on where  $d_j^T$  falls in the distance range:

$$\begin{aligned} w_j^T(d_j^T) &= 0 \quad (d_j^T < -L) \\ w_j^T(d_j^T) &= \left(1 - \left(\frac{d_j^T}{w_j^T}\right)^2\right)^2 \quad (-L \leq d_j^T \leq L) . \\ w_j^T(d_j^T) &= 0 \quad (d_j^T > L) \end{aligned} \quad (6)$$

227 Weights are assigned to each LOS wind velocity value. In the 3rd step, a new first-degree polynomial expression for  
 228 the LSM with the weighted data is estimated as follows.  
 229

$$\begin{aligned}
 a_j' &= \frac{\sum_{i=T-(N-1)}^T w_j^i \sum_{i=T-(N-1)}^T w_j^i z^i W_j^i - \sum_{i=T-(N-1)}^T w_j^i z^i \sum_{i=T-(N-1)}^T w_j^i W_j^i}{\sum_{i=T-(N-1)}^T w_j^i \sum_{i=T-(N-1)}^T w_j^i (z^i)^2 - \left(\sum_{i=T-(N-1)}^T w_j^i z^i\right)^2} \\
 b_j' &= \frac{\sum_{i=T-(N-1)}^T w_j^i z^i \sum_{i=T-(N-1)}^T w_j^i W_j^i - \sum_{i=T-(N-1)}^T w_j^i z^i W_j^i \sum_{i=T-(N-1)}^T w_j^i z^i}{\sum_{i=T-(N-1)}^T w_j^i \sum_{i=T-(N-1)}^T w_j^i (z^i)^2 - \left(\sum_{i=T-(N-1)}^T w_j^i z^i\right)^2}
 \end{aligned} \tag{7}$$

230 This process is repeated until the weight of the error value decreases and converges.  
 231



232  
 233 **Fig. 6 Conceptual explanation of Tuckey's biweight methodology applied to line-of-sight (LOS) wind at various distances.**  
 234 **First step: simple least-squares fit. Second step: observations are compared with the estimate. The data are weighted, and**  
 235 **extreme outliers are excluded, using Eq. (6). Third step: Least-squares fit of the weighted data.**

236  
 237  
 238

## 2.4 Filtering Wind-Velocity Noise

240 Lidar is subject not only to measuring errors and loss of LOS data values but also to random noise; this type  
 241 of noise also leads to a poor estimation of the airflow vector. **The random noise is caused by the reduced intensity of**  
 242 **the received light due to the thin aerosol concentration in the sky. A general Lidar signal consists of random noise**  
 243 **superimposed on the spectral signal. If the signal intensity is low, peak search may only detect the random noise.**  
 244 **(Additional randomness caused by environmental factors and data processing in Lidar is considered here as**  
 245 **randomness of the wind-speed values.)**

246 A simple spline algorithm generates a curve that passes through all sample points; therefore, it is not able to  
247 generate a smooth curve when the sample points have random noise, and a smoothing spline algorithm is often applied  
248 to remove the random noise in the Lidar LOS wind values, as in the study by Woltring, 1986. The curve generated by  
249 this algorithm does not pass through all sample points, and because of that, it can be smoother, even when there is  
250 random noise from Lidar LOS wind measurements. The smoothing spline model minimizes the criterion function  $C_p$ ,

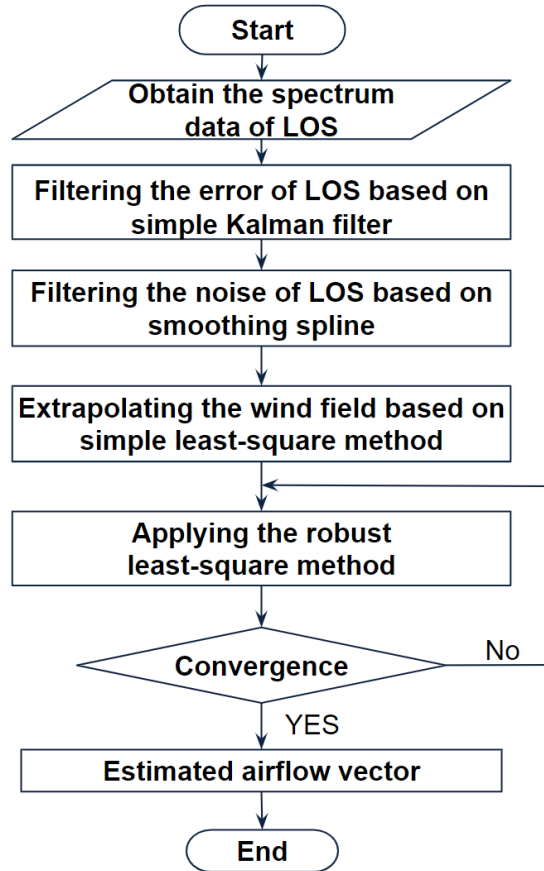
$$C_p = \sum_{i=1}^n v_i \{y_i - s_p(x)\}^2 + p \int \left( \frac{d^2 s_p}{dx^2} \right)^2 dx, \quad (8)$$

251 where  $y_i$  is a sample point value,  $s_p(x)$  is the value generated by a simple spline algorithm,  $v_i$  is a weighted factor, and  
252  $p$  is the regularization parameter. The smoothest curve is generated when the criterion function  $C_p$  is minimized.  
253

## 254 2.5 System Flowchart

255 The airflow-vector estimation algorithm is a sequence of five different processes, which are summarized  
256 below. The system flowchart is shown in [Fig. 7](#).

- 257 1) The filtering algorithm based on a simple Kalman filter is used to remove the error in Lidar LOS  
258 wind-data values.
- 259 2) The smoothing spline method is applied to reduce the negative effect of the random noise in LOS  
260 wind-data values and extrapolates the values at positions for which no measurements can be read. This is identified  
261 as the first-step error.
- 262 3) Extrapolation, based on the polynomial expression, is carried out to estimate the wind-field values  
263 by using current and past LOS wind data.
- 264 4) A robust LSM model is applied to obtain a more accurate polynomial expression. The calculation  
265 repeats until the parameter converges.
- 266 5) The airflow vector is calculated by Eq. (1) with the extrapolated LOS wind.



267

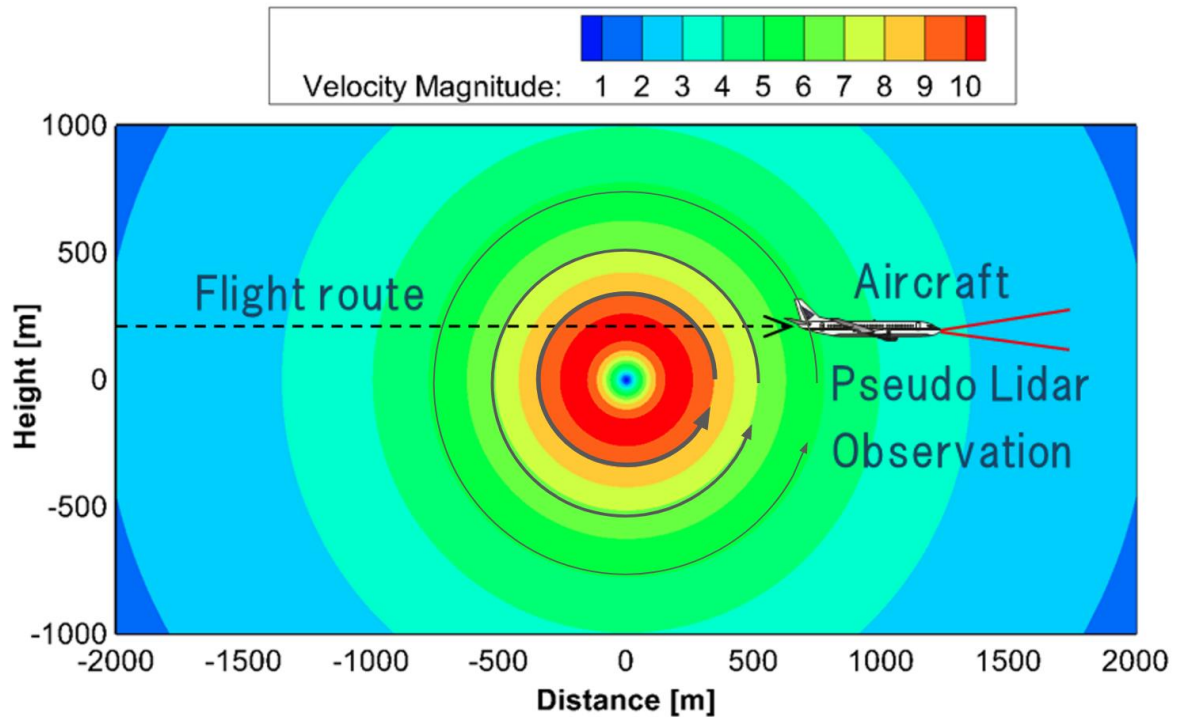
268

**Fig. 7** System flowchart for the airflow vector estimation algorithm

### 269 3 Test Configurations

#### 270 3.1 Ideal Vortex Model

271 We have conducted numerical experiments to evaluate the performance of actual airborne Lidars. The ideal  
 272 vortex model is defined and used to evaluate the estimated performance of the airflow vector. In this study, the  
 273 Hallock-Burnham vortex model (Hinton et al., 1997) is used. The experiment generates a large number of pseudo-  
 274 Lidar values, from which the airflow vector is estimated. The estimation results are then compared with the reference  
 275 wind-field values of the ideal vortex model. **Figure 8** shows the distribution of wind velocity generated using the  
 276 Hallock-Burnham vortex model.



277  
278 **Fig. 8 The distribution of vertical wind velocity generated by the Hallock-Burnham vortex model**

279  
280 **3.2 NWP model**

281 The results predicted by a numerical weather model—the Japan Meteorological Agency Non-Hydrostatic  
282 Model (JMA-NHM)—are used to evaluate airflow-vector estimation performance (Saito et al., 2007; Kikuchi et al.,  
283 2015). To obtain high-resolution weather prediction, a one-way multi-nesting technique (Kikuchi et al. 2015) is  
284 employed for downscaling purposes. The computational domain is nested four times to increase grid resolutions from  
285 5.0 to 0.05 km gradually (in the sequence 5.0, 1.5, 0.5, 0.15, and 0.05 km).

286 Three-hour mesoscale objective analysis data, collected using a mesoscale four-dimensional variational data-  
287 assimilation system at the Japan Meteorological Agency (Saito et al., 2007), are used for the initial condition of 5.0  
288 km grid resolution. The experiment generates a large number of simulated twin-Lidar observation values along flight  
289 routes from the wind-field data generated by JMA-NHM, which are more realistic than ideal-vortex model results.  
290 The airflow vector is estimated from the pseudo-Lidar observations and compared with the JMA-NHM reference field.

291 **Figure 9 shows the distribution of the vertical wind velocity values generated by JMA-NHM.**

292

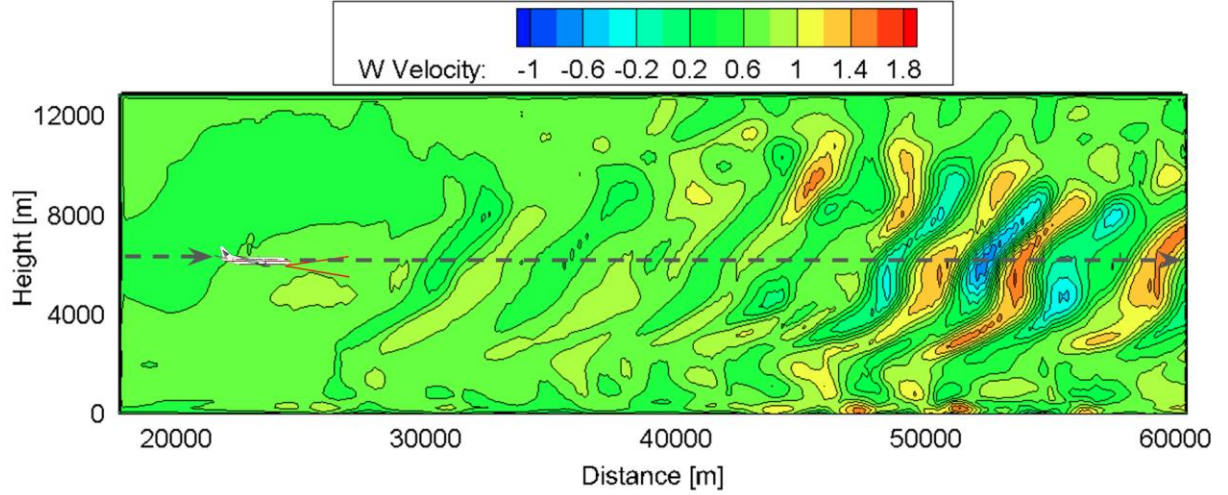


**Fig. 9** Vertical wind velocity distribution map generated by JMA-NHM

### 3.3 Generation of pseudo-errors and noise

To confirm the effectiveness of the proposed filtering algorithms, errors and noise are generated artificially by using the parameter of the backscattering coefficient in the atmosphere and the statistics-based coherent Lidar equation (Kameyama et al., 2007). The backscattering coefficient is strongly related to the aerosol density in the atmosphere, and it has an impact on the Lidar measurements and estimation performance. When the backscattering coefficient is very low, the measurement performance is worse, and the LOS wind data show errors and noise. Apart from this, the measurement performance is related to the focal distance, pulse width, and Lidar power (Kameyama et al., 2007). The signal-noise ratio (SNR) at the receiver, at each LOS distance, is calculated by using the coherent Lidar equation and the detailed operating condition of JAXA's Lidar (Inokuchi and Akiyama 2019):

$$SNR(R) = \frac{\eta P_t \Delta R \beta K^{2R} \frac{\pi D^2}{4R^2}}{h f B SRF(R)} \quad (9)$$

$$SRF(R) = 1 + \left\{1 - \frac{R}{F}\right\}^2 \left\{\frac{k(A_c D)^2}{8R}\right\}^2 + \left\{\frac{A_c D}{2S_0(R)}\right\}^2 \quad (10)$$

$$S_0(R) = (1.1 k^2 R C_n^2)^{-\frac{3}{5}} \quad (11)$$

Here,  $R$  is the observation distance,  $\eta$  is the system efficiency,  $P_t$  is the light-transmission power,  $\Delta R$  is the resolution range,  $\beta$  is the backscattering coefficient,  $K$  is the atmospheric transmittance,  $D$  is the opening size of the optical antenna,  $h$  is Planck's constant,  $f$  is optical frequency,  $B$  is received bandwidth,  $F$  is focal distance,  $k$  is wave number,  $A_c$  is the vignetting factor of the optical antenna, and  $C_n^2$  is the atmospheric structure constant. In this study, the conditions are set according to the design specification for airborne Lidars. Six atmospheric conditions are prepared in order to evaluate the filtering performance. The backscattering coefficients are (standard case)  $1.8 \times 10^{-8} \text{ sr}^{-1}\text{m}^{-1}$ , (a)  $1.8 \times 10^{-11} \text{ sr}^{-1}\text{m}^{-1}$ , (b)  $1.35 \times 10^{-11} \text{ sr}^{-1}\text{m}^{-1}$ , (c)  $0.9 \times 10^{-11} \text{ sr}^{-1}\text{m}^{-1}$ , (d)  $0.45 \times 10^{-11} \text{ sr}^{-1}\text{m}^{-1}$ , and (e)  $0.18 \times 10^{-11} \text{ sr}^{-1}\text{m}^{-1}$ . Figure 10 shows the statistics for the error and noise as functions of SNR bandwidth.

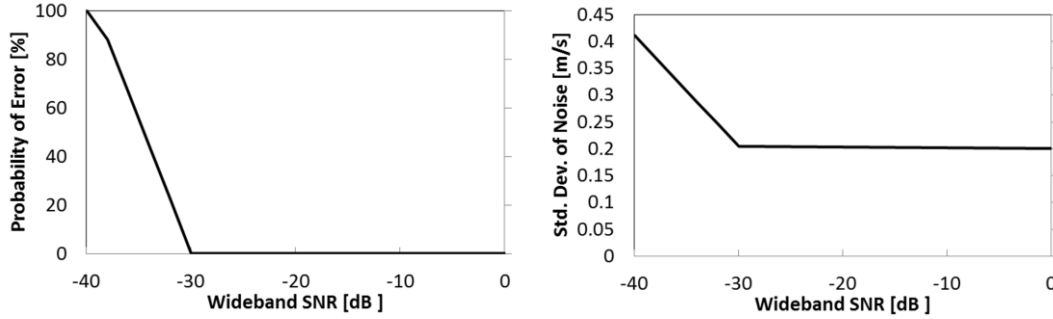


**Fig. 10** Probability of error and standard deviation of noise as functions of signal-noise ratio (SNR) bandwidth

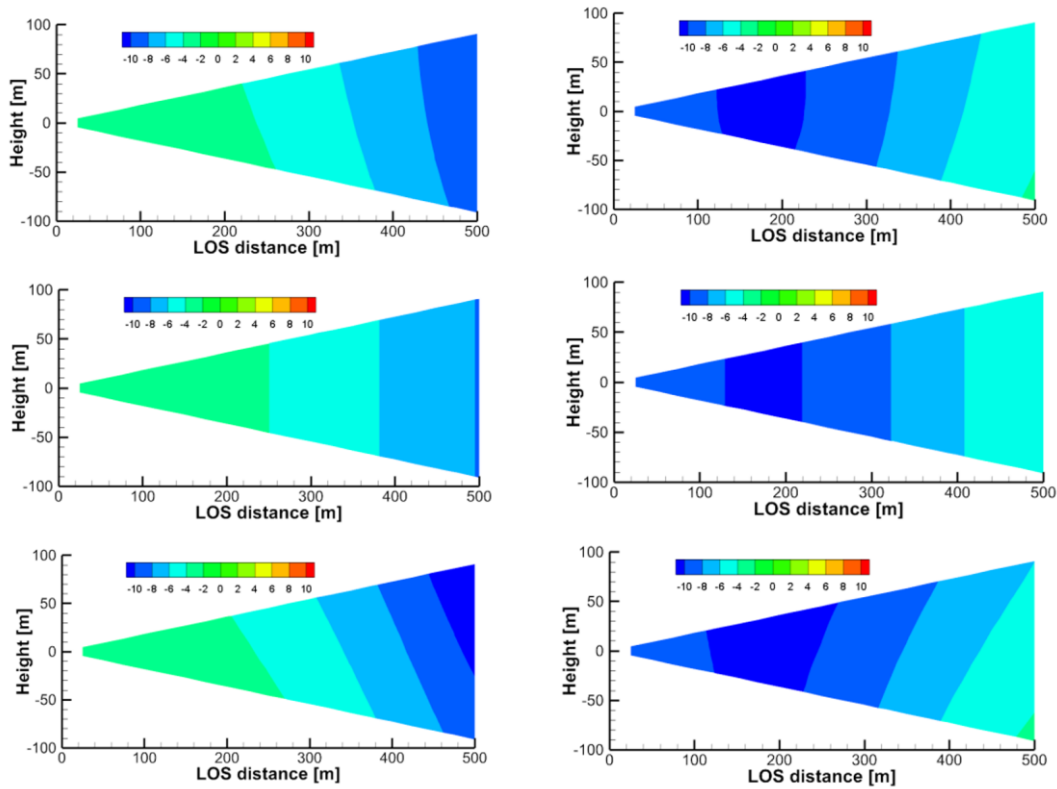
## 4 Results

### 4.1 Ideal Vortex Model without Error and Noise

The numerical experiments with the ideal vortex model have been carried out, and Figs. 11 and 12 show the distributions of the horizontal and vertical wind components that are estimated by the simple vector conversion and the proposed method. The flights start at the edge of the computational space. Figs. 11 and 12 show the results after 10 and 15 s, respectively. Thus, they represent the instants of time before and during the aircraft's close approach to the vortex core. As shown in Figs. 11 and 12, the simple vector conversion method, which assumes that the wind field of the region between the Lidars is homogeneous, cannot accurately reproduce the two-dimensional distribution between the Lidars. On the other hand, the figures confirm that the proposed method can estimate the two-dimensional distribution of wind-field values between the Lidars. Figure 11 shows that the two-dimensional distribution obtained with the proposed method is very similar to that of the reference field. In addition, the results show that the horizontal wind velocity with simple vector conversion is approximately  $-7$  m/s, whereas that with the proposed method is  $-9.5$   $\text{ms}^{-1}$ ; the horizontal wind velocity of the reference field is  $-9.0$   $\text{ms}^{-1}$  at LOS distance of 450–500 m. Figure 12 shows that the results of the horizontal and vertical wind velocities with simple vector conversion are considerably lower than those of the reference field. The horizontal wind results show that the value obtained with the simple vector conversion is approximately  $-9.5$   $\text{ms}^{-1}$ , whereas that with the proposed method is approximately  $-3.5$   $\text{ms}^{-1}$ ; the horizontal wind velocity of the reference field is approximately  $-4.5$   $\text{ms}^{-1}$  at LOS distance of 450–500 m. The vertical wind results show that the value obtained with simple vector conversion is approximately  $-1.0$  m/s, whereas that obtained with the proposed method is approximately  $8.5$   $\text{ms}^{-1}$ ; the vertical wind velocity of the reference field is approximately  $7.0$   $\text{ms}^{-1}$  at LOS distance of 450–500 m. Therefore, simple vector conversion has significantly large errors between the reference and estimated values. The errors in both the horizontal and vertical wind values estimated by the proposed method are much smaller than those estimated with simple vector conversion. Although the two-dimensional distribution of the horizontal wind-field values of the proposed method is larger than that of the reference field at a LOS distance of 450–500 m, the vertical wind-field values can provide a good assessment of the reference field shown in Fig. 12. The 15 s timing in Fig. 12 is a more challenging case than others because the aircraft is positioned very close to the center of the vortex, and the wind direction changes abruptly. Although it is difficult to

342 estimate the perfect wind-field value at this time by using the proposed method, the proposed estimation method  
 343 demonstrably has a much higher accuracy than simple vector conversion. Overall, the proposed method has much  
 344 better performance than the simple vector conversion method, and it can estimate the two-dimensional distribution of  
 345 wind field values accurately, unlike the simple vector conversion method.

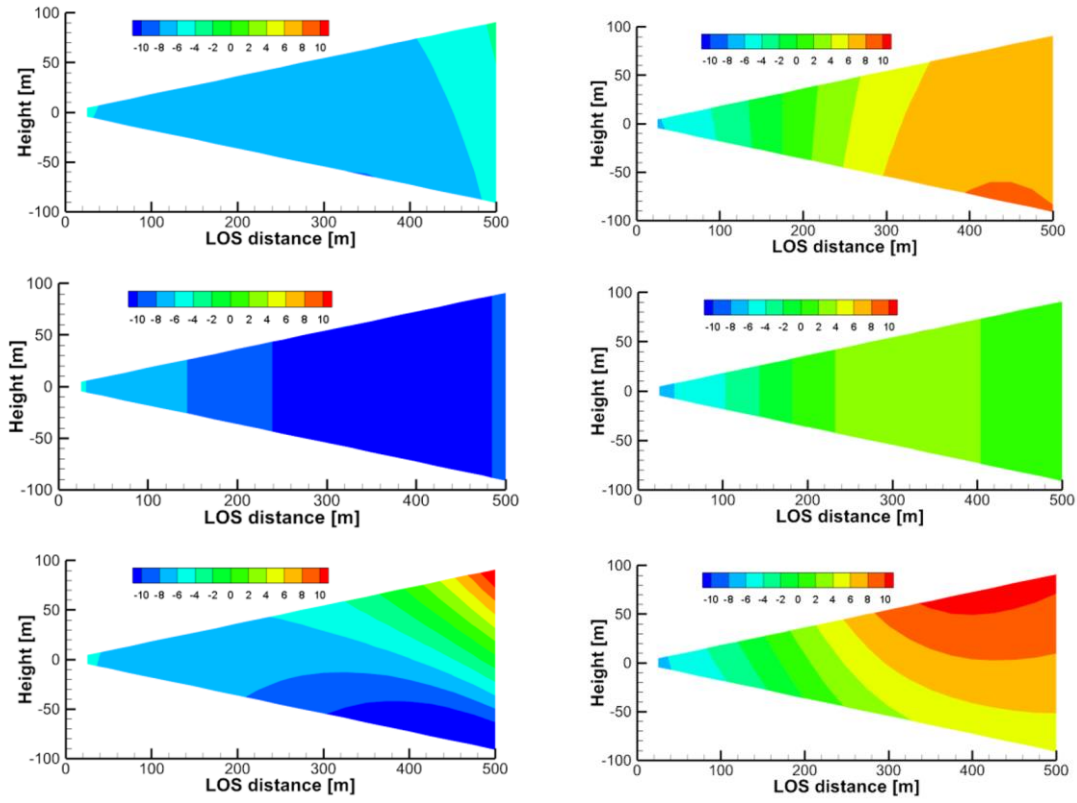
346 **Next, the statistical estimation performance is evaluated using 100 pseudo-routes that are randomly generated**  
 347 **750 m above and below the center of the vortex core; Fig. 13 shows the results for the vertical wind values, along with**  
 348 **the performance required for automatic control. The root mean square error (RMSE) between the reference-field value**  
 349 **and the estimated wind-field value is used for evaluating the estimation performance. Moreover, the effect of the**  
 350 **number of past Lidar observations used to determine the wind field, i.e., the past LOS wind, is checked. Simple vector**  
 351 **conversion cannot satisfy the performance requirement at a LOS distance greater than 350 m. This means that**  
 352 **achieving preview control using the simple vector conversion method may be difficult. At a LOS distance of 500 m,**  
 353 **the RMSEs of the vertical wind values of the simple vector conversion and proposed methods are approximately 4.0**  
 354 **ms<sup>-1</sup> and 1.2 ms<sup>-1</sup>, respectively. The proposed method can cater to the performance demand even if the number of past**  
 355 **LOS wind values used is different; a lower number leads to better estimation performance.**



356  
 357 **Fig. 11 Distributions of the horizontal and vertical wind components estimated by the simple vector conversion method**  
 358 **vs. the proposed method (at time 10 s). Upper figures: ideal vortex model; middle figures: simple vector conversion**  
 359 **method; lower figures: proposed method with five-past LOS wind datasets. Left figures: horizontal wind values; right**  
 360 **figures: vertical wind values**

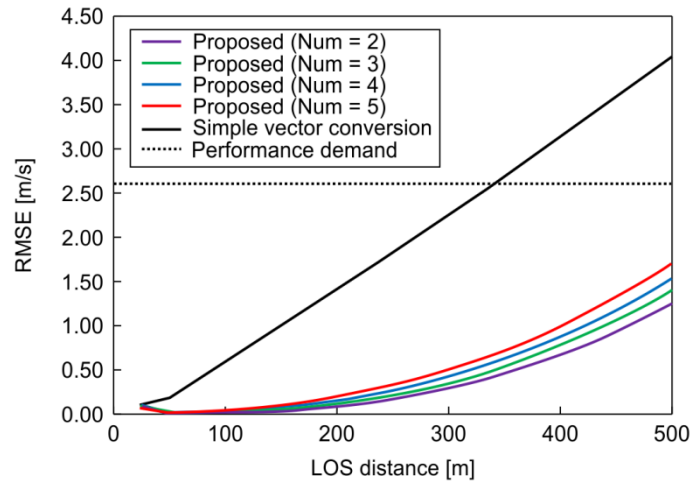
361





362  
363  
364  
365  
366

**Fig. 12** Distributions of the horizontal and vertical wind components estimated by the simple vector conversion method vs. the proposed method (at time 10 s). Upper figures: ideal vortex model; middle figures: simple vector conversion method; lower figures: proposed method with five-past LOS wind datasets. Left figures: horizontal wind values; right figures: vertical wind values



367  
368  
369

**Fig. 13** Statistical estimation performance (root mean square error) of vertical wind values (ideal vortex model). Num = number of past line-of-sight (LOS) wind values used

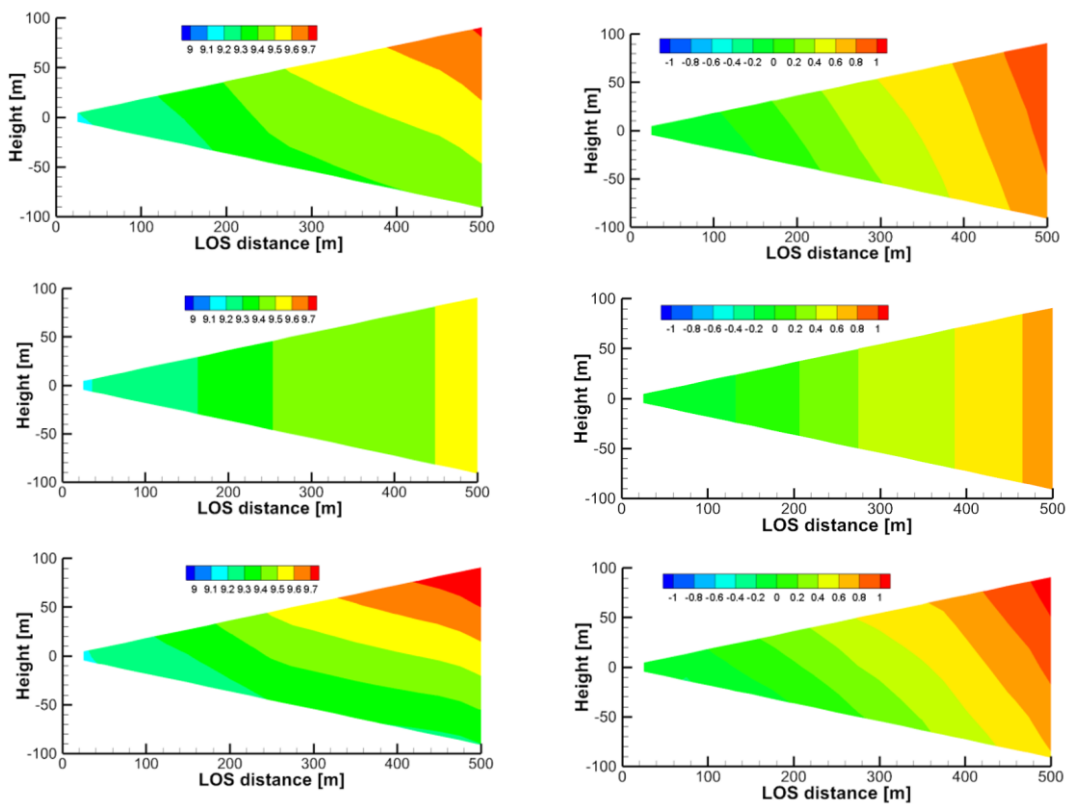
370 **4.1 Numerical Weather Prediction without Error and Noise**

371 We also conducted numerical experiments with NWP values. Figs. 14 and 15 show the distributions of the  
372 horizontal and vertical wind components that are estimated by simple vector conversion and the proposed method.

373 Figure 14 shows the results for the instants of time **before and during the approach to a vertical wind fluctuation**. The  
 374 simple vector conversion method cannot accurately reproduce the two-dimensional distribution of the wind field  
 375 between the Lidars. On the other hand, the proposed method can estimate the two-dimensional distribution of the wind  
 376 field between the Lidars more accurately. Figure 15 shows that the wind velocities predicted by the simple vector  
 377 conversion method are higher than the reference fields at 300-500 m of LOS distance, in contrast to those of the  
 378 proposed method.

379 **Next, the statistical estimation performance is evaluated using 100 pseudo-routes that are randomly generated**  
 380 **between 2 km and 10 km altitude**. Fig. 16 shows the results, along with the performance requirement for automatic  
 381 control. The effect of the number of past LOS wind-values used is also checked. In this case, both simple vector  
 382 conversion and the proposed method can satisfy the performance demand for preview control; however, the  
 383 performance results of simple vector conversion are much worse than those of the proposed method. Moreover, the  
 384 proposed method can estimate quite accurate wind-field values. In this case, the use of a higher number of past LOS  
 385 wind values leads to better estimation performance.

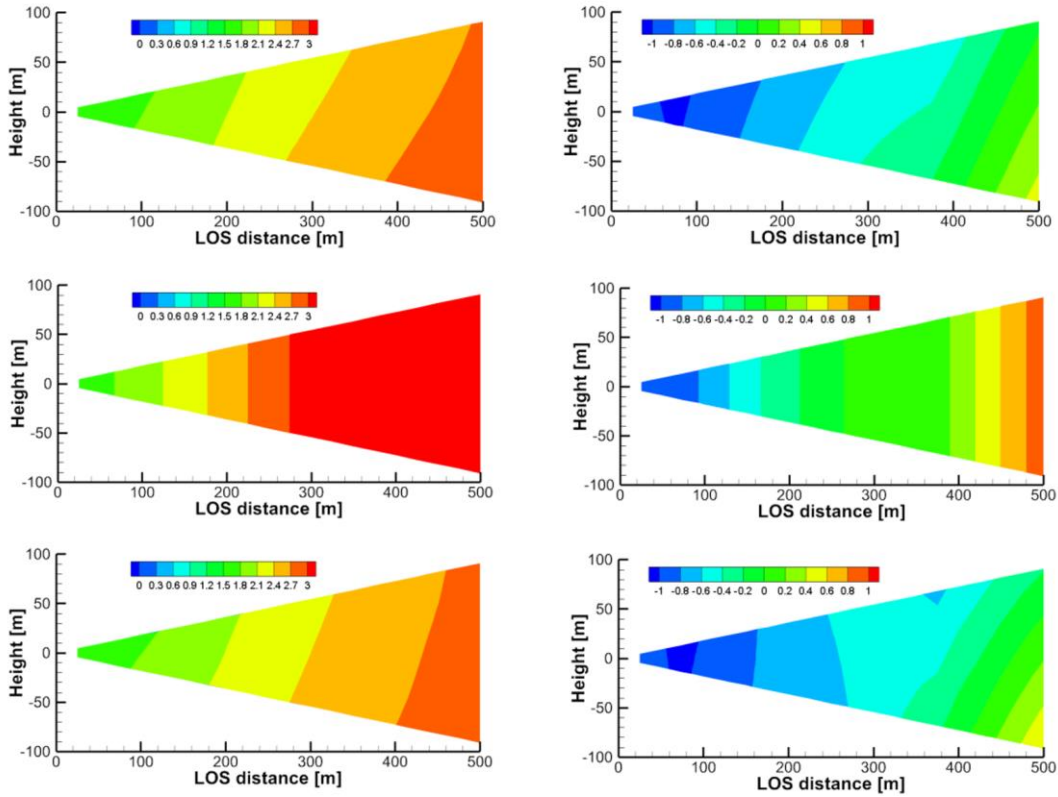
386



387

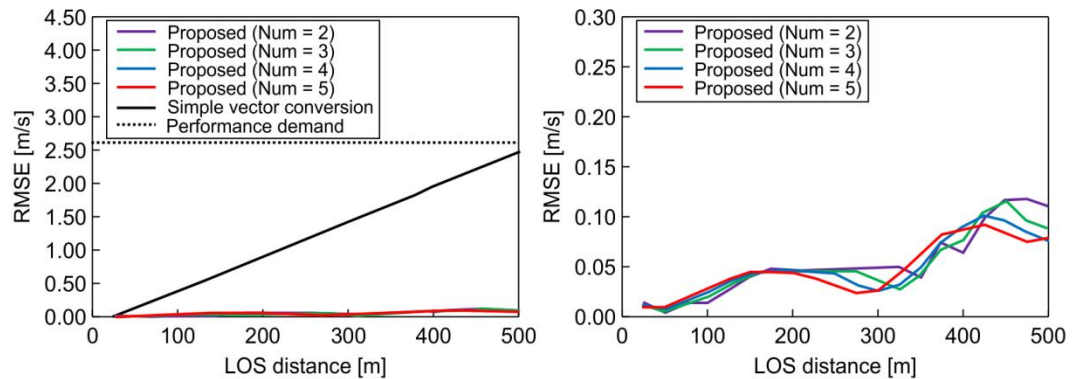
388 **Fig. 14 Distributions of horizontal and vertical wind components estimated via simple vector conversion and proposed**  
 389 **method before approach to vertical wind fluctuation. Upper figures: ideal vortex model; middle figures: simple vector**  
 390 **conversion method; lower figures: proposed method with five-past LOS wind datasets. Left figures: horizontal wind**  
 391 **values; right figures: vertical wind values**

392



393  
 394 **Fig. 15 Distributions of horizontal and vertical wind components estimated via simple vector conversion and proposed**  
 395 **method immediately during approach to vertical wind fluctuation. Upper figures: ideal vortex model; middle figures:**  
 396 **simple vector conversion method; lower figures: proposed method with five-past LOS wind datasets. Left figures:**  
 397 **horizontal wind values; right figures: vertical wind values**

398



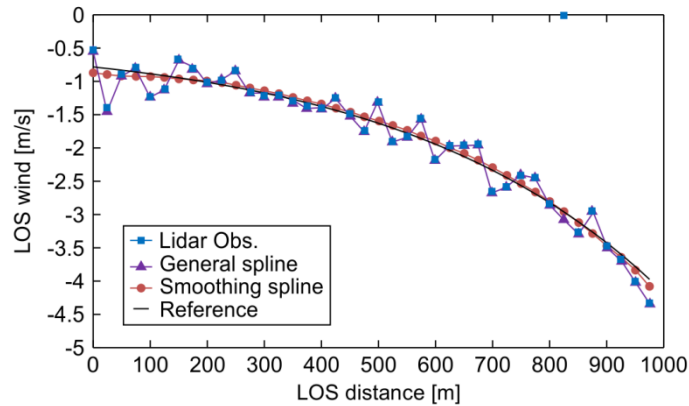
399  
 400 **Fig. 16 Statistical estimation performance (root mean square error) for numerical weather prediction results. Num =**  
 401 **number of past line-of-sight (LOS) wind values used**

#### 402 4.2 Ideal vortex model with error and noise

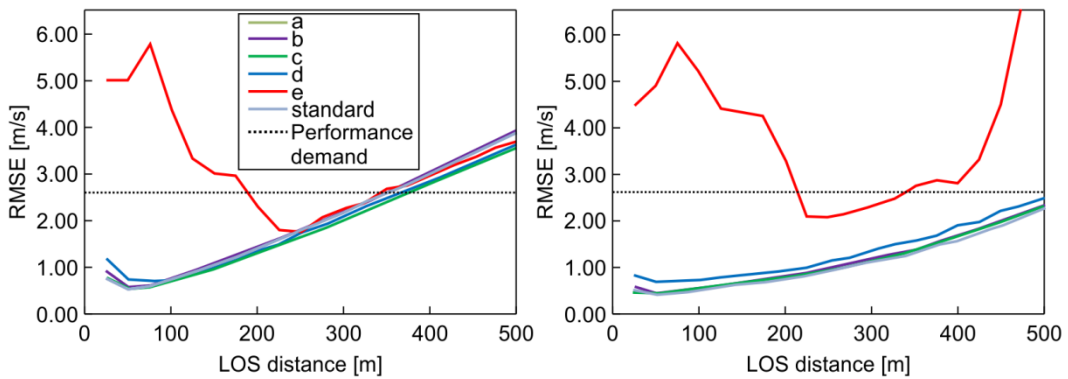
403 In this section, numerical experiments with error and noise in LOS wind values are conducted to evaluate the  
 404 estimation performance of the proposed method. These numerical experiments show the error/noise-filtering

405 performance difference between simple vector conversion and the proposed method with extrapolation from the past  
 406 LOS wind. Six atmospheric conditions are prepared in order to evaluate the filtering performance. The backscattering  
 407 coefficients are (standard case)  $1.8 \times 10^{-8} \text{ sr}^{-1} \text{ m}^{-1}$ , (a)  $1.8 \times 10^{-11} \text{ sr}^{-1} \text{ m}^{-1}$ , (b)  $1.35 \times 10^{-11} \text{ sr}^{-1} \text{ m}^{-1}$ , (c)  $0.9 \times 10^{-11} \text{ sr}^{-1} \text{ m}^{-1}$ , (d)  
 408  $0.45 \times 10^{-11} \text{ sr}^{-1} \text{ m}^{-1}$ , and (e)  $0.18 \times 10^{-11} \text{ sr}^{-1} \text{ m}^{-1}$ .

409 First, numerical experiments with the ideal vortex model are carried out. Figure 17 shows the LOS wind  
 410 values, which include the measured data with error and noise, the reference wind, the smoothing spline, and the general  
 411 spline model results. Figure 17 shows that the smoothing spline can filter the error and noise data of LOS wind values.  
 412 When the general spline is used, the error can be filtered correctly by using a simple Kalman filter and a robust LSM;  
 413 however, the noise cannot be filtered. Next, the statistical estimation performance is evaluated using 100 pseudo-  
 414 routes that are randomly generated 750 m above and below the center of the vortex core. Fig. 18 shows the results of  
 415 the statistical estimation performance with error and noise. In addition, the difference due to the atmospheric  
 416 conditions in the six cases with different backscattering coefficients is also checked. Simple vector conversion cannot  
 417 satisfy the performance demand at a distance farther than 350 m LOS and cannot work correctly under atmospheric  
 418 condition (e). The proposed method can always satisfy the performance demand except under atmospheric condition  
 419 (e). It thus shows much better performance than simple vector conversion, even though it is difficult to estimate the  
 420 wind field values by either method for atmospheric condition (e), which contains much larger noise levels than the  
 421 other conditions.



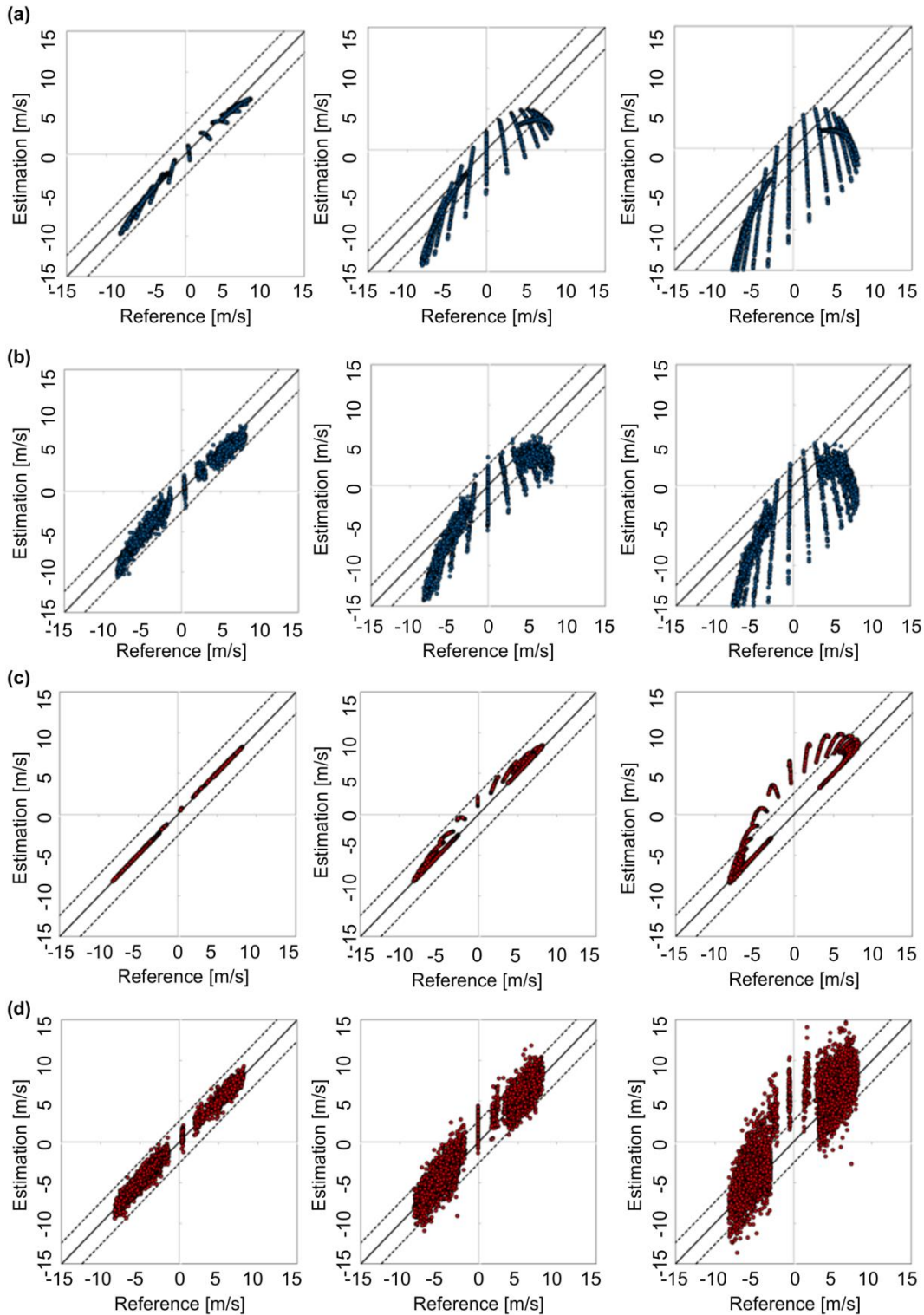
422  
 423 **Fig. 17 Line-of-sight (LOS) wind values: measured data with error and noise, reference wind, smoothing spline, and**  
 424 **general spline**



425

426 **Fig. 18 Statistical estimation performance (root mean square error) for line-of-sight (LOS) wind velocities including error**  
427 **and noise under six atmospheric-condition scenarios (a–e and standard) (assuming ideal vortex model). Left figure:**  
428 **simple vector conversion; right figure: proposed method**

429 In addition, the cross-plots of the reference and the estimated vertical wind are shown as Fig. 19. In Figs. 19  
430 (a) and (b) the results of the simple vector conversion are presented; (c) and (d) show the results of the proposed  
431 method. Figs. 19 (a) and (c) are the cases without error and noise, **whereas (b) and (d) are the cases with error and**  
432 **noise**. By comparing (a) and (c), we can deduce that the proposed method provides a much better estimation than does  
433 simple vector conversion. The results in (b) and (d) are spread wider than those in (a) and (c), because of the noise  
434 data of LOS wind values. It is worth mentioning that the noise data have more negative effects on the result at 500 m  
435 LOS distance than at 100 m and 300 m LOS. Nevertheless, comparison of (b) and (d) shows that the proposed method  
436 can provide more accurate estimations than the simple vector conversion method.



437

438 **Fig. 19** Cross-plots of the reference and the estimated vertical wind data. Left figures: 100 m line-of-sight (LOS) distance;  
 439 middle figures: 300 m LOS distance; right figures: 500 m LOS distance. (a), (b): Simple vector conversion; (c), (d):  
 440 proposed method. (a), (c): cases without error and noise; (b), (d): cases with error and noise. The dots indicate the wind  
 441 speed estimated at 5 Hz, and the dotted lines indicate the performance demand for control.

442

### 4.3 Numerical weather prediction with error and noise

We also carry out numerical experiments with NWP. The statistical estimation performance is conducted by using 100 pseudo-routes between 2 km and 10 km altitude. Fig. 20 shows the results of the statistical estimation performance with error and noise. Six different atmospheric conditions (standard, (a), (b), (c), (d), and (e), defined by their backscattering coefficients) are used. In this case, both simple vector conversion and the proposed method can satisfy the performance requirement for preview control; however, the simple vector conversion shows worse performance than the proposed method. The proposed method can estimate wind-field values quite accurately and displays better performance than the simple vector conversion method. As in the previous experiment, it is difficult to estimate the wind field-values for atmospheric condition (e) by using either simple vector conversion or the proposed method.

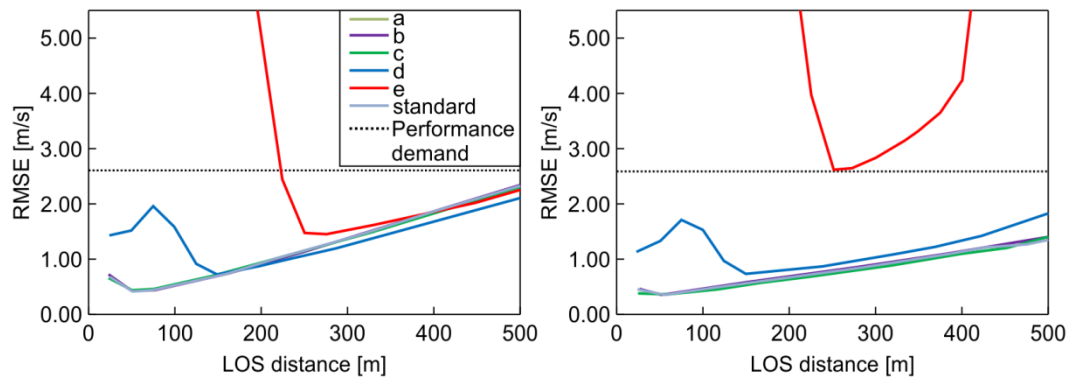


Fig. 20 Statistical estimation performance (root mean square error) for line-of-sight (LOS) wind velocities (including error and noise) under six atmospheric-condition scenarios (a–e and standard) with numerical weather-prediction data. Left figure: simple vector conversion; right figure: proposed method

## 5. Conclusion

In this study, an airflow vector estimation algorithm based on upward and downward airborne Lidars has been proposed for preview control to prevent turbulence-induced aircraft accidents. This estimation algorithm uses the technique of extrapolating the wind-field values by using the LSM and the current and past LOS wind datasets to improve the accuracy of estimated wind values. Two test configurations for numerical experiments (ideal vortex flow and realistic NWP weather field values) have been used to evaluate the estimation of the airflow vector.

Numerical experiments on LOS wind estimation show that the proposed extrapolation method has much better performance than simple vector conversion methods, and it can estimate the two-dimensional distribution of wind-field values accurately, which simple vector conversion cannot. The estimation performance and the computational cost of the proposed method can satisfy the performance demand for preview control.

Numerical experiments with error and noise in the LOS wind data have been conducted to evaluate the performance of the proposed estimation method. These numerical experiments show that the smoothing spline model can filter noise correctly and reduce its negative effects. The proposed method performs much better than the simple vector conversion method, although it is difficult to estimate the wind-field values for atmospheric condition (e) with either method. Atmospheric condition (e) has more noise than other conditions, and when the noise exceeds a certain level, it becomes difficult to estimate the air flow regardless of the method applied.

473 The proposed algorithm can satisfy the performance demands for preview control in both estimation  
474 performance and computational cost. It can estimate a two-dimensional distribution that cannot be estimated by  
475 existing methods. This is valuable for improving the accuracy of the preview control: for example, the proposed  
476 method can cope with the critical case where the flight direction of the aircraft is at a steep angle with the aircraft  
477 either ascending or descending.

478 The findings of this study are subject to certain limitations. The target size of the atmospheric turbulence is  
479 assumed by the proposed algorithm to be comparable to or larger than the observation region between the Lidars.  
480 Therefore, it is difficult to estimate a wind field with turbulence smaller than this. The effect on the aircraft vibration  
481 due to such minor turbulence, however, is minimal. **An exception to this is aircraft-generated wake turbulence, which  
482 still poses a safety risk. The radius of the actively fluctuating wake-turbulence core is only a few meters, so the  
483 proposed method could lead to erroneous predictions.** A second limitation is that the current results are obtained from  
484 numerical experiments and not from evaluations of actual observations. **Currently, the Lidar system is being modified  
485 to be smaller and lighter in order to suit small experimental aircraft. The onboard Lidar system and real-time airflow-  
486 vector estimation will be validated by flight experiments in 2021; the whole gust-alleviation system, including preview  
487 control, will be demonstrated in 2022. The results of this research will be applied to this flight demonstration.**

488  
489

#### 490 **Author Contributions**

491 Ryota Kikuchi, Takashi Misaka, and Shigeru Obayashi designed the experiments. Ryota Kikuchi performed  
492 the experiments, developed the model code, performed the simulations, and prepared the manuscript with  
493 contributions from all co-authors. Hamaki Inokuchi contributed to the analysis and interpretation of data related to  
494 Lidar and assisted in the preparation of the manuscript. All authors approve the final version of the manuscript and  
495 agree to be accountable for all aspects of the work in ensuring that questions related to the accuracy or integrity of any  
496 part of the work are appropriately investigated and resolved.

#### 497 **Competing Interests**

498 The authors declare that they have no conflict of interest.

#### 499 **References**

500 Airbus S.A.S.: Flight Operations Briefing Notes: Adverse Weather Operations – Optimum Use of the Weather Radar,  
501 available at: <https://safetyfirst.airbus.com/optimum-use-of-weather-radar/>, 2020, last access: 22 September 2020.  
502  
503 Barny, H.: DELICAT – Demonstration of Lidar Based Clear Air Turbulence Detection, in: Innovation for Sustainable  
504 Aviation in a Global Environment: Proceedings of the Sixth European Aeronautics Days, 253, 2012.



505  
506 Boeing Commercial Airplanes: Statistical Summary of Commercial Jet Airplane Accidents, 2018.  
507  
508 Federal Aviation Administration: Preventing injuries caused by turbulence 2006, available at:  
509 [https://www.faa.gov/regulations\\_policies/advisory\\_circulars/index.cfm/go/document.information/documentid/99831](https://www.faa.gov/regulations_policies/advisory_circulars/index.cfm/go/document.information/documentid/99831),  
510 2020, last access: 23 September 2020.  
511  
512 Fezans, N., Joos, H.D., and Deiler, C.: Gust load alleviation for a long-range aircraft with and without anticipation,  
513 CEAS Aeronautical Journal, 10, 1-25, 2019.  
514  
515 Hamada, Y.: New LMI-based conditions for preview feedforward synthesis, Control Engineering Practice, 90, 19-26,  
516 2019  
517  
518 Hinton, D. A., and Tatnall, C. R.: A candidate wake vortex strength definition for application to the NASA aircraft  
519 vortex spacing system (AVOSS), NASA Technical Reports, 1997.  
520  
521 Huber, P. J.: Robust Statistics, Springer, Berlin, Heidelberg, 2008.  
522  
523 Inokuchi, H.: Detection of the Clear Air Turbulence by an Airborne Doppler LIDAR, in: Proceedings of Asia-Pacific  
524 International Symposium on Aerospace Technology, 2012.  
525  
526 Inokuchi, H. and Akiyama, T.: True airspeed measured by an airborne coherent doppler lidar, in: APISAT 2019: Asia  
527 Pacific International Symposium on Aerospace Technology (p. 554), 2019.  
528  
529 Inokuchi, H., Tanaka, H., and Ando, T.: Development of an onboard doppler lidar for flight safety, Journal of Aircraft,  
530 46(4), 1411-1415, 2009  
531  
532 International Air Transportation Association: Safety Report 2015, 2016.  
533  
534 Japan Transport Safety Board: 2003-2012: Aircraft accident reports, available at: <http://www.mlit.go.jp/jtsb/>, 2020,  
535 last access: 23 September 2020.  
536  
537 Kikuchi, R., Misaka, T., and Obayashi, S.: Real-Time Flow Prediction of Low-Level Atmospheric Turbulence, in  
538 33rd Wind Energy Symposium, 2015.  
539  
540 Kameyama, S., Ando, T., Asaka, K., Hirano, Y., and Wadaka, S.: Compact all-fiber pulsed coherent Doppler lidar  
541 system for wind sensing, Applied Optics, 46(11), 1953-1962, 2007

542  
543 Kim, J.H. and Chun, H.Y.: Statistics and possible sources of aviation turbulence over South Korea. *Journal of Applied*  
544 *Meteorology and Climatology*, 50(2), 311-324, 2011.  
545  
546 Kim, J. H., Chun, H. Y., Sharman, R. D., and Keller, T. L.: Evaluations of upper-level turbulence  
547 diagnostics performance using the Graphical Turbulence Guidance (GTG) system and pilot reports  
548 (PIREPs) over East Asia, *Journal of Applied Meteorology and Climatology* 50(9), 1936-1951, 2011.  
549  
550 Kim, J. H., Chan, W. N., Sridhar, B., and Sharman, R. D.: Combined winds and turbulence prediction  
551 system for automated air-traffic management applications, *Journal of Applied Meteorology and*  
552 *Climatology* 54(4), 766-784, 2015.  
553  
554 Machida, S.: Project Overview of R&D for Onboard Turbulence Detection System, in: Proceedings of Asia-Pacific  
555 International Symposium on Aerospace Technology 2017, Plenary Lecture 4, Seoul, Korea, 2017.  
556  
557 Misaka, T., Nakabayashi, F. K., Obayashi, S., and Inokuchi, H.: Filtering Algorithm of Airborne Doppler Lidar  
558 Measurements for Improved Wind Estimation, *Transactions of the Japan Society for Aeronautical and Space Sciences*,  
559 58(3), 149-155, 2015  
560  
561 Neininger, B.: Trends in airborne atmospheric observations, *European Meteorological Society Annual Meeting 2017*,  
562 14, EMS2017-322, 2017  
563  
564 Newsom, R. K., et al.: Validating precision estimates in horizontal wind measurements from a Doppler lidar, US  
565 Department of Energy, Office of Scientific and Technical Information, NREL/JA-5000-68401,  
566 <https://doi.org/10.5194/amt-10-1229-2017>, 2017.  
567  
568 Regan, C.D., and Jutte, C.V.: Survey of applications of active control technology for gust alleviation and new  
569 challenges for lighter-weight aircraft. NASA Technical Memorandum, NASA-TM-2012-216008, 2012.  
570  
571 Saito, K., Ishida, J. I., Aranami, K., Hara, T., Segawa, T., Narita, M., and Honda, Y.: Nonhydrostatic atmospheric  
572 models and operational development at JMA, *Journal of the Meteorological Society of Japan* 85B, 271-304, 2007.  
573  
574 Sakimura, T., Watanabe, Y., Ando, T., Kameyama, S., Asaka, K., Tanaka, H., Yanagisawa, T., Hirano,  
575 Y. and Inokuchi, H.: 3.2 mJ, 1.5  $\mu\text{m}$  laser power amplifier using an Er, Yb:glass planar  
576 waveguide for a coherent Doppler LIDAR, in: Proceedings of 17th Coherent Laser Radar  
577 Conference, Barcelona, Spain, 2013.  
578

579 Schmitt, N. P., Rehm, W., Pistner, T., Zeller, P., Diehl, H., and Navé, P.: The AWIATOR airborne LIDAR turbulence  
580 sensor, *Aerospace Science and Technology*, 11(7), 546-552, 2007  
581

582 Sermi, F., Cuccoli, F., Mugnai, C., and Facheris, L.: Aircraft hazard evaluation for critical weather avoidance, in:  
583 *IEEE Metrology for Aerospace (MetroAeroSpace)*, Benevento, Italy, 2015, 454-459, 2015.  
584

585 **Sharman, R., Tebaldi, C., Wiener, G., and Wolff, J.: An integrated approach to mid-and upperlevel**  
586 **turbulence forecasting, *Weather and Forecasting* 21(3), 268–287, 2006.**  
587

588 Soreide, D. C., Bogue, R. K., Ehernberger, L. J., Hannon, S. M., and Bowdle, D. A.: Airborne coherent LIDAR for  
589 advanced in-flight measurements (ACLAIM) flight testing of the LIDAR sensor, *NASA Technical Reports*, 2000.  
590

591 **Wei, T., Xia, H., Hu, J., Wang, C., Shangguan, M., Wang, L., Jia, M. and Dou, X.: Simultaneous wind and rainfall**  
592 **detection by power spectrum analysis using a VAD scanning coherent Doppler lidar, *Optics Express*, 27(22), 31235-**  
593 **31245, 2019.**  
594

595 **Williams, P.D.: Increased light, moderate, and severe clear-air turbulence in response to climate change, *Advances in***  
596 ***Atmospheric Sciences*, 34(5), 576-586, 2017.**  
597

598 Woltring, H. J.: A Fortran package for generalized, cross-validatorspline smoothing and differentiation, *Advances*  
599 *in Engineering Software*, 8(2) 104-113, 1986.